

University of Wollongong - Research Online

Thesis Collection

Title: Analysis of lepton contamination in high energy x-ray beams

Author: Nyanpen Damrongkijudom

Year: 2007

Repository DOI:

Copyright Warning

You may print or download ONE copy of this document for the purpose of your own research or study. The University does not authorise you to copy, communicate or otherwise make available electronically to any other person any copyright material contained on this site.

You are reminded of the following: This work is copyright. Apart from any use permitted under the Copyright Act 1968, no part of this work may be reproduced by any process, nor may any other exclusive right be exercised, without the permission of the author. Copyright owners are entitled to take legal action against persons who infringe their copyright. A reproduction of material that is protected by copyright may be a copyright infringement. A court may impose penalties and award damages in relation to offences and infringements relating to copyright material.

Higher penalties may apply, and higher damages may be awarded, for offences and infringements involving the conversion of material into digital or electronic form.

Unless otherwise indicated, the views expressed in this thesis are those of the author and do not necessarily represent the views of the University of Wollongong.

Research Online is the open access repository for the University of Wollongong. For further information contact the UOW Library: research-pubs@uow.edu.au

2007

Analysis of lepton contamination in high energy x-ray beams

Nyanpen Damrongkijudom
University of Wollongong

Follow this and additional works at: <https://ro.uow.edu.au/theses>

University of Wollongong

Copyright Warning

You may print or download ONE copy of this document for the purpose of your own research or study. The University does not authorise you to copy, communicate or otherwise make available electronically to any other person any copyright material contained on this site.

You are reminded of the following: This work is copyright. Apart from any use permitted under the Copyright Act 1968, no part of this work may be reproduced by any process, nor may any other exclusive right be exercised, without the permission of the author. Copyright owners are entitled to take legal action against persons who infringe their copyright. A reproduction of material that is protected by copyright may be a copyright infringement. A court may impose penalties and award damages in relation to offences and infringements relating to copyright material.

Higher penalties may apply, and higher damages may be awarded, for offences and infringements involving the conversion of material into digital or electronic form.

Unless otherwise indicated, the views expressed in this thesis are those of the author and do not necessarily represent the views of the University of Wollongong.

Recommended Citation

Damrongkijudom, Nuanpen, Analysis of lepton contamination in high energy x-ray beams, PhD thesis, School of Engineering Physics, University of Wollongong, 2007. <http://ro.uow.edu.au/theses/738>

NOTE

This online version of the thesis may have different page formatting and pagination from the paper copy held in the University of Wollongong Library.

UNIVERSITY OF WOLLONGONG

COPYRIGHT WARNING

You may print or download ONE copy of this document for the purpose of your own research or study. The University does not authorise you to copy, communicate or otherwise make available electronically to any other person any copyright material contained on this site. You are reminded of the following:

Copyright owners are entitled to take legal action against persons who infringe their copyright. A reproduction of material that is protected by copyright may be a copyright infringement. A court may impose penalties and award damages in relation to offences and infringements relating to copyright material. Higher penalties may apply, and higher damages may be awarded, for offences and infringements involving the conversion of material into digital or electronic form.

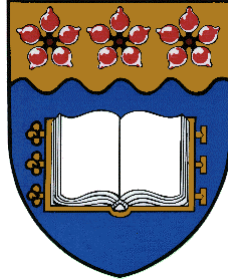
ANALYSIS OF LEPTON CONTAMINATION IN HIGH ENERGY X-RAY BEAMS

A thesis submitted in fulfillment of the requirements for the award of
the degree

DOCTOR OF PHILOSOPHY

from

UNIVERSITY OF WOLLONGONG



by

Nuanpen Damrongkijudom, M.S. (Medical Physics)

School of Engineering Physics

University of Wollongong

Wollongong, Australia

August 2007

CERTIFICATION

I, Nuanpen Damrongkijudom, declare that this thesis, submitted in fulfilment of the requirements for the award of Doctor of Philosophy, in the School of Engineering Physics, University of Wollongong, is wholly my own work unless otherwise referenced or acknowledged. The document has not been submitted for qualifications at any other academic institution.

Nuanpen Damrongkijudom

6 August 2007

ABSTRACT

The objectives of this study were to improve our understanding of the contamination arising in conventional radiotherapy treatment from the various principal processes involved. The evolution of the contamination was investigated in two main ways: i) experimental measurements; and ii) the Monte Carlo method.

The magnetic field strengths in this improved design were intended to result in more uniform magnetic flux densities in the area of interest, with the prediction of a greater volume where the electron contamination was effectively removed by our magnetic deflector device. The magnetic field strengths obtained by the magnetic deflector will theoretically give rise to electron deflection radii that should cause the majority of electron contamination to exit the treatment field. An enhancement of the electron dose was never experimentally observed in the irradiated area, and a percentage reduction of the skin and subcutaneous dose up to 34 % with the NdFeB magnetic device was seen for a 20 x 20 cm² field size. The elimination of significant electron doses due to contaminant electrons down to a depth of a few millimetres was obtained with this newly designed magnetic deflector device.

In the study, the experiments were verified by an Attix chamber and radiographic film. The surface dose was increased as the field size was increased in an open field and when a Perspex tray was placed in the beam, with the increase especially significant in the case where there was both a Perspex tray and a larger field size. The Perspex tray or a wedge filter eliminate secondary electrons and generate new electrons at the same time, however, when combined with magnetic field the surface dose is reduced significantly. Results are also shown for the surface dose profile in two dimensions (x and y-axis) with the surface dose showing a decrease at all sites within the treatment field due to the magnetic deflector device, not only for an open field, but also when a wedge or a Perspex tray is in the beam.

Calculation and analysis of spectra of deflected electrons in photon beams from the linear accelerator treatment head were investigated. Calculating such spectra with more accuracy requires knowledge of the characteristics of the electron beam incident on the target as well as better equipment for modelling the linear accelerator. We used the

Monte Carlo method performed with BEAMnrc and DOSXYZnrc code to derive estimates for the average energy deposited in the system. Monte Carlo modelling of photon beams was achieved and adjusted for two parameters: $AE = ECUT = 0.521 \text{ MeV}$ and $AE = ECUT = 0.700 \text{ MeV}$ by matching the Monte Carlo calculated depth dose and beam profile data with the measured data.

The capability of the Monte Carlo program in evaluating dose distribution has been verified by comparison with measurements in a water phantom and with radiographic film. The comparisons were performed for percentage of the build-up dose for various field sizes. Ionisation measurements were made in a solid water phantom by means of an Attix chamber for experiments to determine the dose in the build-up region. The measurement of skin dose uses an Attix parallel plate ionisation chamber, which is primarily used as the benchmark chamber in solid-water phantom dose build-up measurements.

Monte Carlo simulations were performed to generate data to predict the dose distribution for 6 MV x-rays. Investigation of dose components of electron spectra are compared between calculated and measured dose distributions. From the Monte Carlo calculations and measurements on the surface and in the build-up region for 6 MV x-ray beams based on our results, we conclude that our optimised simulation model represents the beam emerging from the treatment head and the calculated percentage depth doses in such a way that there is a satisfactory match with the experimental measurements for the same irradiation set-ups.

TABLE OF CONTENTS

CERTIFICATION	i
ABSTRACT	ii
LIST OF FIGURES	x
LIST OF TABLES	xxi
ACKNOWLEDGEMENTS	xxiii
CHAPTER 1 INTRODUCTION	1
1.1. Lepton contamination in high-energy x-ray beams	1
1.2. The statement of problems from the contamination electrons	2
1.3. Consideration of a proposed technique	3
1.4. Aim and objectives	4
1.5. Scope	4
CHAPTER 2 SURFACE DOSE IN HIGH ENERGY X-RAY BEAMS	6
2.1. Introduction	6
2.1.1. Surface dose	7
2.1.2. Build-up region	8
2.1.3. D_{\max} (The Maximum Dose)	10
2.1.4. d_{\max} (The Depth of Maximum Dose)	10
2.1.5. PDD (Percentage depth dose)	11
2.2. High-energy x-ray beams from linear accelerators	11
2.3. High energy x-ray beams Interactions	13
2.3.1. Photoelectric Effect Interaction	13
2.3.2. Compton Effect Interaction	14

2.3.3. Pair production Interaction	15
2.3.4. Thomson scattering	16
2.3.5. Photodisintegration	16
2.4. Contamination Electrons	16
2.4.1. Source from treatment head materials	19
2.4.2. Source from treatment setup parameters	19
2.5. Skin dose	19
2.6. Surface dose from high energy x-ray beams for different clinical set-up parameters	20
2.6.1. Using beam modifying and accessory devices	21
2.6.2. Source to Surface Distance	22
2.6.3. Angle of incident beam	23
2.7. Magnetic field	24
2.8. Electron deflection in magnetic field	25
2.8.1. Motion of a charged particle in a magnetic field	25
2.8.2. Direction of particle's motion is changed	26
2.8.3. Speed unchanged in the magnetic field	26
2.8.4. Uniform circular motion in a magnetic field	26
2.8.5. Helical motion in a magnetic field	27
CHAPTER 3 MATERIALS AND METHODS	31
3.1. Linear accelerator	31
3.1.1. Linear accelerator treatment head	33
3.2. Ionisation chambers	34
3.2.1. The Attix chamber	36

3.3.	Phantom materials	37
3.3.1.	Solid Water phantom	37
3.4.	Beam modifying device	39
3.4.1.	Wedges	39
3.4.2.	Perspex tray	40
3.5.	Film dosimetry	41
3.5.1.	Radiographic film	43
3.5.2.	Types of radiographic film	44
3.5.3.	Radiographic film density	45
3.6.	Film digitiser	46
3.7.	Hall Effect Teslameter	48
3.8.	Neodymium iron boron magnetic deflector	50
3.9.	Monte Carlo technique	52
3.9.1.	Monte Carlo technique for modelling linear accelerator	53
CHAPTER 4	RESULTS AND DISCUSSION	55
4.1.	Magnetic Deflection Model	55
4.1.1.	Magnetic deflector device	56
4.1.2.	Simulation of magnetic fields around magnetic deflector device	57
4.1.3.	Measurement of magnetic fields around magnetic deflector device	59
4.1.4.	Simulation and measurement of the magnetic field	61
4.1.5.	Dose in the build up region with magnetic deflector device	65
4.1.6.	Conclusions on magnetic fields produced by deflector device	68

4.2. Electron deflection in magnetic field	69
4.2.1. Analytical Theory	70
4.2.2. Electron deflection using magnetic deflection device	75
4.2.3. Conclusion on magnetic deflection	82
4.3. Surface dose measurement in magnetic field	82
4.3.1. Film dosimetry and calibration method	83
4.3.2. Extrapolation Technique	83
4.3.3. Extrapolated surface dose of 6 MV x-rays with magnetic device	94
4.3.4. Conclusion on surface dose measurement	100
CHAPTER 5 LEPTON CONTAMINATION IN 6 MV X-RAYS	101
5.1. Electron contamination from high-energy x-ray beams	105
5.2. Source of electron contaminate	106
5.3. Experimental set up	107
5.4. Results and discussion of measurement	109
5.4.1. Dose build up region	109
5.4.2. Field size	112
5.4.3. Beam modifying devices	118
5.4.4. Surface dose from Attix chamber and radiographic film	125
5.5. Conclusions	126
CHAPTER 6 MONTE CARLO CALCULATIONS	128
6.1. Introduction	128
6.2. Monte Carlo approach to electron contamination sources in Varian Clinac 2100C	128

6.3. METHODS and MATERIALS	131
6.3.1. Monte Carlo method	131
6.3.2. Linear accelerators	134
6.3.3. Monte Carlo simulation	139
6.4. Results and Discussion	141
6.4.1. Linear accelerator head	141
6.4.2. Contaminant particles	149
6.5. Characteristics of radiation from a linear accelerator head	151
6.5.1. Methods and Materials	153
6.5.2. Results and Discussion	154
6.6. Monte Carlo Depth dose distribution	158
6.6.1. Methods and Materials	158
6.6.2. Results and Discussion	161
6.7. Conclusions	169
CHAPTER 7 EXPERIMENTS AND MONTE CARLO CALCULATION	171
7.1. Experimental setup	172
7.1.1. Dose build-up region	172
7.1.2. Radiographic film with magnetic deflection device	173
7.2. Monte Carlo method	174
7.2.1. Water phantom	175
7.2.2. Radiographic film	175
7.3. Results and Discussion	177
7.3.1. Dose in the build-up region	177

7.3.2. Surface dose	189
7.3.3. Electron and contamination doses	194
7.4. Conclusions	200
CHAPTER 8 CONCLUSIONS	201
8.1. Magnetic field model	201
8.2. Electron contamination from 6 MV x-ray beams	202
8.3. Monte Carlo Simulation	206
8.3.1. Monte Carlo simulation model	206
8.3.2. Determination of the transport model parameters	209
REFERENCES	212

LIST OF FIGURES

Figure 2.1	Some of the characteristics from a general central axis percent depth dose curve	7
Figure 2.2	Build-up curves in polystyrene for 10 x 10 cm ² open fields for the photon beams studied	9
Figure 2.3	Dose build-up curves for Clinac 6 MV x-ray beams at 100 cm SSD for fields of 5 x 5 cm ² to 40 x 40 cm ²	9
Figure 2.4	Depth of d _{max} as a function of field size for 6, 10 and 18 MV x-rays	10
Figure 2.5	Percentage depth dose of 10 and 25 MV x-ray beams for field sizes of 10 x 10 cm ² and 35 x 35 cm ² at 100 cm SSD	11
Figure 2.6	The diagram illustrates the structure of the linear accelerator treatment head	13
Figure 2.7	The Photoelectric Effect interaction process	14
Figure 2.8	The Compton Effect interaction process	14
Figure 2.9	The pair production interaction process	15
Figure 2.10	Relative absorbed dose at phantom surface for 21 MV x-rays, with filter thickness of 2 g / cm ² for field sizes of 10 x 10 cm ² , 20 x 20 cm ² , and 40 x 40 cm ²	16
Figure 2.11	The diagram illustrates the structure of the linear accelerator treatment head and the regions where electron contamination is produced	17
Figure 2.12	Cross-section of the skin anatomy shows the main structures in the epidermis and dermis layers	20
Figure 2.13	The electron contribution from the portion of the ERS determining the surface dose from the incident photon beams	23
Figure 2.14	The magnetic field lines between the poles of two bar magnets, displayed using the Vizimag program	25
Figure 2.15	The direction of the magnetic force is always at right angle to the plane formed by the velocity vector (v) and the magnetic field (B) for positive and negative charged particles	26

Figure 2.16	A charged particle moving parallel to the magnetic field will travel with a uniform velocity, and there is no work on the charged particle	27
Figure 2.17	Trigonometry is used to resolve the velocity of a charged particle into components parallel to (\hat{v}_p) and perpendicular to (\hat{v}_\perp) the magnetic field lines	28
Figure 2.18	The path of a charged particle with components of velocity both parallel and perpendicular to the field direction in a uniform magnetic field is helical	28
Figure 2.19	The radius as a function of electron energy from 0.5 to 6 MeV in different magnetic field strengths	29
Figure 3.1	Diagram of the medical linear accelerator system used to produce x-ray beams	32
Figure 3.2	Picture of Varian Clinac 2100C linear accelerator. This machine is capable of producing 6 and 18 MV x-ray beams and 6, 9, 12, 16, and 20 MeV electron beams	32
Figure 3.3	Diagram showing the structure of a medical linear accelerator treatment head	34
Figure 3.4	Picture of the Attix model 449 chamber (Gammex RMI Model 457) used for the experiments in solid water	36
Figure 3.5	The ratio of the mass energy-absorption coefficient relative to water of Solid Water as a function of x-ray beam energy	38
Figure 3.6	Solid Water phantoms with various slab thicknesses used for the experiments	39
Figure 3.7	Picture of wedges with 15, 30, 45, and 60 degree angles that were used in the experiments	40
Figure 3.8	Picture of 6 mm thickness Perspex tray used in the experiments	41
Figure 3.9	The ratio of the mass energy-absorption coefficient of photographic emulsion to that of water as a function of the x-ray beam energy	42
Figure 3.10	Dose profile of radiographic film compared with dose to water	43
Figure 3.11	A cross-sectional view of radiographic film layers	45
Figure 3.12	Pictures of X Omat V films for the measurement of dose	46

Figure 3.13	The major components of the film digitiser	47
Figure 3.14	Picture of Vidar VXR-12 Plus film digitiser for scanning film	47
Figure 3.15	The Hall Effect for magnetic field measurement	48
Figure 3.16	The Hall Effect probe is direction dependent, and the output is greatest when the flux lines are perpendicular to it	49
Figure 3.17	Pictures of the DTM-132 Digital Teslameter and Hall probe	50
Figure 3.18	Picture of Neodymium Iron Boron (NdFeB) lanthanide ceramic magnet each of dimensions 5 x 5 x 5 cm and 5 x 5 x 1.25 cm were selected for placement in an Aluminium holding frame as the magnetic deflector device	51
Figure 3.19	NdFeB magnetic deflector device inserted directly into an accessory mount in a linear accelerator head	52
Figure 4.1	The magnetic deflector in location for simulated clinical measurements	55
Figure 4.2	Schematic diagram of the details of the magnetic deflector device with a photograph of the actual device	56,57
Figure 4.3	(a) Magnetic field lines through the central plane of our magnetic deflector as determined by Vizimag. (b) Greyscale colour-intensity image of the magnetic field intensity (magnitude) around the magnetic deflector	58
Figure 4.4	The 3D assumption made by Vizimag	59
Figure 4.5	(a) The measurement performed at a distance of $x = -7.5$ cm, (b) at the central plane ($x = 0$), and (c) performed at distance of $x = 7.5$ cm away from the central plane.	60,61
Figure 4.6	Simulation of Y-component magnetic field strength using Vizimag within the 10 cm pole separation along the y-axis on the magnetic deflector central plane	62
Figure 4.7	Measurement of magnetic field strength along the y-axis on the magnetic deflector central plane within the 10 cm pole separation. Curves represent data taken at different depths along the z-axis, down to 10 cm	62
Figure 4.8	The central measurement and simulation plane and a 3D surface mesh plot of the Y-components	63

Figure 4.9	Variation between the experimental data and the Vizimag prediction in the central plane	64
Figure 4.10	Y-direction magnetic field strength between the magnet banks on axes other than the central one	65
Figure 4.11	Measurements for open field (without deflector) and with the field when the magnetic deflector device in place for 6 MV x-ray beams in the build-up region	67,68
Figure 4.12	Diagram of the locations of the component modules in medical linear accelerator machine with magnetic deflector device	70
Figure 4.13	Magnetic deflector device with the magnetic field (\vec{B}) parallel to the y-axis	71
Figure 4.14	The diagram for the deflection of an electron after passing through the magnetic field region	74
Figure 4.15	The experimental set-up, with the magnetic device attached to the treatment head of the linear accelerator by placement under the block tray location and with the radiographic film placed perpendicular to the beam axis	76
Figure 4.16	(a) The deflection distance and angle of electrons as a function of electron energy from 0.5 to 20 MeV in different magnetic field strengths using simplified model of uniform magnetic field distribution calculated by Vizimag	77
	(b) The deflection distance and angle of electrons as a function of electron energy from 0.5 to 20 MeV in different magnetic field strengths measured data of the magnetic field strength of magnetic deflector device	78
Figure 4.17	Radiographic images used to determine deflection distances of electron beams from 6 MeV up to 20 MeV after passing through the magnetic deflector device	80
Figure 4.18	Surface dose can be obtained from a second order polynomial extrapolation from radiographic film for field size 10 x 10 cm ² , 15 x 15 cm ² and 20 x 20 cm ² with and without magnetic field	84,85
Figure 4.19	Dose profiles measured cross-plane without (open field) magnetic deflection for a field size of 10 x 10 cm ² at the surface and at 0.38, 1.14, and 1.9 mm depths	86
Figure 4.20	Dose profiles measured cross-plane with magnetic deflection for a field size of 10 x 10 cm ² at the surface and at 0.38, 1.14, and 1.9	87

mm depths

Figure 4.21	Dose profiles measured in-plane without (open field) magnetic deflection for a field size of $10 \times 10 \text{ cm}^2$ at the surface and at 0.38, 1.14, and 1.9 mm depths	88
Figure 4.22	Dose profiles measured in-plane with magnetic deflection for a field size of $10 \times 10 \text{ cm}^2$ at the surface and at 0.38, 1.14, and 1.9 mm depths	89
Figure 4.23	Dose profiles measured cross-plane without (open field) magnetic deflection for a field size of $20 \times 20 \text{ cm}^2$ at the surface and at 0.38, 1.14, and 1.9 mm depths	90
Figure 4.24	Dose profiles measured cross-plane with magnetic deflection for a field size of $20 \times 20 \text{ cm}^2$ at the surface and at 0.38, 1.14, and 1.9 mm depths	91
Figure 4.25	Dose profiles measured in-plane without (open field) magnetic deflection for a field size of $20 \times 20 \text{ cm}^2$ at the surface and at 0.38, 1.14, and 1.9 mm depths	92
Figure 4.26	Dose profiles measured in-plane with magnetic deflection for a field size of $20 \times 20 \text{ cm}^2$ at the surface and at 0.38, 1.14, and 1.9 mm depths	93
Figure 4.27	Radiographic images of 6 MV beams of the three layers of film for field sizes of $10 \times 10 \text{ cm}^2$, $15 \times 15 \text{ cm}^2$, and $20 \times 20 \text{ cm}^2$ illustrate that the electron contamination is swept away by the magnetic field	94
Figure 4.28	Surface dose can be obtained from a second order polynomial extrapolation from radiographic film	95
Figure 4.29	Extrapolated surface dose profile at central axis for 6 MV, measured cross-plane and in-plane with and without (open field) magnetic field from the deflector for a radiation field size of $10 \times 10 \text{ cm}^2$	97
Figure 4.30	Extrapolated surface dose profile at central axis for 6 MV, measured cross-plane and in-plane with and without (open field) magnetic field from the deflector for a radiation field size of $15 \times 15 \text{ cm}^2$	98
Figure 4.31	Extrapolated surface dose profile at central axis for 6 MV, measured cross-plane and in-plane with and without (open field) magnetic field from the deflector for a radiation field size of $20 \times 20 \text{ cm}^2$	99

Figure 5.1	(a) Radiographic image with Surface and Profile plots present the lepton contamination of an open field (without deflection or beam-modifying devices) of $10 \times 10 \text{ cm}^2$ (b) Radiographic image with Surface and Profile plots present the lepton contamination with magnetic field. Electrons and positrons are swept in opposite directions following the Lorentz force rule	102,103 104,105
Figure 5.2	Source size and location of electron contamination in a linear accelerator head; ΔY is the upper jaw opening and ΔX is the lower jaw opening	107
Figure 5.3	Diagram of the linear accelerator with magnetic deflector device and radiographic film as used in the experiments	108
Figure 5.4	Percentage dose build up for 6 MV x-rays from an Attix chamber (open field) and in magnetic field for field sizes of $10 \times 10 \text{ cm}^2$, $15 \times 15 \text{ cm}^2$, and $20 \times 20 \text{ cm}^2$	110
Figure 5.5	Percentage contamination dose reduction for 6 MV x-rays from an Attix chamber with a magnetic field applied to a linear accelerator treatment head for $10 \times 10 \text{ cm}^2$, $15 \times 15 \text{ cm}^2$, and $20 \times 20 \text{ cm}^2$ field sizes	111
Figure 5.6	Extrapolated surface doses from radiographic films are shown for profiles measured in-plane and cross-plane of 6 MV x-ray beam for open field, tray in place, and magnetic field and tray in place with magnetic field for field sizes of (a) $5 \times 5 \text{ cm}^2$, (b) $10 \times 10 \text{ cm}^2$, (c) $20 \times 20 \text{ cm}^2$, and (d) $30 \times 25 \text{ cm}^2$	113,114 115,116
Figure 5.7	Relative surface dose from radiographic film of 6 MV x-rays for open field and 6 mm Perspex tray with and without magnetic field for $5 \times 5 \text{ cm}^2$, $10 \times 10 \text{ cm}^2$, $20 \times 20 \text{ cm}^2$, and $30 \times 25 \text{ cm}^2$ field sizes	119
Figure 5.8	Extrapolated surface doses are shown for profiles measured in-plane and cross-plane for 6 MV x-ray beam with magnetic field for wedge field with a wedge angle of (a) $W15^\circ$, (b) $W30^\circ$, (c) $W45^\circ$, and (d) $W60^\circ$ compared with open field	120,121 122,123
Figure 6.1	Schematic drawing of linear accelerator components modelled in Monte Carlo simulations	137
Figure 6.2	Schematics of the geometry illustrating the accelerator head components	138

Figure 6.3	Influence of AE on the spectrum for a 6 MV beam for a) all particles and photons after passing through mirror, b) electrons after passing through mirror	143
Figure 6.4	Influence of AE on the spectrum for a 6 MV beam for a) all particles and photons, b) electrons at SSD5100 cm	144
Figure 6.5	Influence of AE on the fluence along the X-axis for a 6 MV beam for a) all particles and photons after passing through the mirror, b) electrons after passing through mirror	146
Figure 6.6	Influence of AE on the fluence along the X-axis for a 6 MV beam for a) all particles and photons after passing through air at 100 cm, b) electrons after passing through air at 100 cm	147
Figure 6.7	Mean energy distribution of a 10 x 10 cm ² 6 MV photon beam simulated along the x-axis after passing through the linear accelerator treatment head at 100 cm for a) all particles and photons, b) electrons	148
Figure 6.8	Influence of AE values on spectral distribution and fluence of particle and electron contamination along the X-axis of 6 MV beam at 100 cm SSD for 10 x 10 cm ² field size: a) spectral distribution of particle and electron contamination, b) fluence of particle and electron contamination	150
Figure 6.9	Influence of AE values on fluence of contaminant particles along the X-axis of 6 MV beam at a) scoring plane after mirror material, b) 100 cm SSD for 10 x 10 cm ² field size	151
Figure 6.10	Schematic representation of a linear accelerator with the photon radiation originating from the accelerator head, passing through the air, and propagating this radiation down to the phantom	152
Figure 6.11	A schematic of the modelling process for each scoring plane for the phase-space information for Monte Carlo calculations of radiation from a linear accelerator treatment head	153
Figure 6.12	Spectral distribution of all particles and photons in (a), (c), (e), (g), (h), (i), (j), (k), electrons and contamination in (b), (d), (f) from a Varian Clinac 2100 C with a 6 MV beam	157
Figure 6.13	Schematic drawing of linear accelerator for the DOSXYZnrc simulation	159

Figure 6.14	Spectral distribution from BEAMnrc phase-space data (AE = 0.700 MeV) of linear accelerator head at 100 cm from the target using BEAMDP calculations of field sizes 5 x 5 cm ² , 10 x 10 cm ² , 20 x 20 cm ² , and 30 x 30 cm ² for a) photon fluence, b) electron fluence	160
Figure 6.15	Monte Carlo calculations using AE = 0.700 MeV to calculate the percent dose build-up distribution for 6 MV Clinac 2100 C for field sizes: a) 5 x 5 cm ² , b) 10 x 10 cm ² , c) 20 x 20 cm ² , d) 30 x 30 cm ²	161
Figure 6.16	Monte Carlo calculation (AE = 0.700 MeV) in the build-up region for 6 MV Clinac 2100 C for field sizes of 5 x 5 cm ² , 10 x 10 cm ² , 20 x 20 cm ² , and 30 x 30 cm ²	162
Figure 6.17	Surface dose profile plot calculated from Monte Carlo (AE = 0.700 MeV) results with field sizes 5 x 5 cm ² , 10 x 10 cm ² , 20 x 20 cm ² , and 30 x 30 cm ² in: (a) distance along the X –axis, and (b) distance along the Y-axis	164
Figure 6.18	Dose distribution on central axis of 6 MV Clinac 2100 C for field size of 10x10 cm ² at AE = 0.521 and 0.700 MeV in a water phantom: a) depth dose distribution, b) dose in the build-up region	165
Figure 6.19	Electron dose distribution on central axis of 6 MV Clinac 2100 C for field size of 10x10 cm ² for AE = 0.521 and AE = 0.700 MeV in a water phantom: a) electron distribution in the build-up region, b) electron depth dose distribution	166
Figure 6.20	Total dose profile plot at different depths in a water phantom for AE = 0.521 and 0.700 MeV from 6 MV Clinac 2100 C for field size of 10 x 10 cm ² along the X and Y-axes	168
Figure 6.21	Electron dose profile plot at different depths for AE = 0.521 and 0.700 MeV for 6 MV beam in a water phantom along the X and Y-axes	168
Figure 7.1	Schematic drawing of linear accelerator for the DOSXYZnrc simulation in a water phantom	176
Figure 7.2	Schematic drawing of the size of scoring voxels for the DOSXYZnrc simulation in the radiographic film on a water phantom	176
Figure 7.3	Match between experimental data and Monte Carlo calculation in the build-up region for a 6 MV beam in a water phantom for AE	178

and ECUT = 0.700 MeV for field sizes of: a) 10 x 10 cm², b) 15 x 15 cm², c) 20 x 20 cm²

Figure 7.4	Match between experimental data and Monte Carlo calculation in the build-up region for 6 MV beam in a water phantom for a field size of 10 x 10 cm ² for AE = 0.521 and 0.700 MeV	182
Figure 7.5	Dose values measured with Attix chamber and Monte Carlo calculations with AE = 0.700 MeV in the build-up region for 6 MV beam in a water phantom for field size of 10 x 10 cm ² : a) Comparison of open (without magnetic field) and magnetic field results for all particles and photons, b) Difference between open and magnetic field results compared to difference between all particles and photons, and percentage of contamination of the total dose	184
Figure 7.6	Dose values measured with Attix chamber and Monte Carlo calculations with AE = 0.700 MeV in the build-up region for 6 MV beam in a water phantom for a field size of 20 x 20 cm ² : a) Open and magnetic field results are compared for all particles and photons, b) Difference between open and magnetic field results compared to difference between all particles and photons, and percentage contamination from the total dose	185
Figure 7.7	Depth dose curves from Monte Carlo results on simulated radiographic film for the energy cut-offs and AE = 0.521 MeV for 6 MV beam and field size of 10 x 10 cm ² : a) depth dose curves of all particles, b) dose distribution of electrons	186
Figure 7.8	Depth dose curves from Monte Carlo calculations on simulated radiographic film for the energy cut-offs and AE = 0.700 MeV for 6 MV beam with field size of 10 x 10 cm ² : a) depth dose curves of all particles, b) dose distribution of electrons	187
Figure 7.9	Comparison of depth dose curves from Monte Carlo calculations on simulated radiographic film using the different AE for 6 MV beam for field size of 10 x 10 cm ² : a) depth dose curves of all particles, b) dose distribution of electrons	188
Figure 7.10	Simulated dose profiles compared between using AE = 0.700 MeV in a water phantom and radiographic film for 6 MV Clinac 2100 C with a field size of 10 x 10 cm ² at different depths along X and Y – axis directions	190
Figure 7.11	Simulated dose profiles compared between using AE = 0.521 MeV in a water phantom and radiographic film for 6 MV Clinac 2100 C for field size of 10 x 10 cm ² at different depths along the X and Y – axes	190

Figure 7.12	Simulated dose profiles compared between using AE = 0.521 MeV and AE = 0.700 MeV on a water phantom for 6 MV Clinac 2100 C for a field size of 10 x 10 cm ² at different depths along the X and Y – axes	191
Figure 7.13	Simulated profiles compared between using AE = 0.521 MeV and AE = 0.700 MeV for radiographic film on a water phantom for 6 MV Clinac 2100 C for a field size of 10 x 10 cm ² for different depths along the X and Y – axes	191
Figure 7.14	Surface dose profiles comparing the MC calculations with measurements on radiographic film using AE = 0.700 MeV for a 6 MV beam along the X and Y– axes for field sizes of: a) 5 x 5 cm ² , b) 10 x 10 cm ² , and c) 15 x 15 cm ²	192
Figure 7.15	Surface dose profiles comparing the MC calculations with measurements on radiographic film using AE = 0.521 and 0.700 MeV for a 6 MV beam along the X and Y– axes for a field size of 10 x 10 cm ²	193
Figure 7.16	Comparison of electron and contamination depth dose curves from Monte Carlo calculations on radiographic film using the different AE for a 6 MV beam with a field size of 10 x 10 cm ² : a) AE = 0.521 MeV, b) AE = 0.700 MeV, c) AE = 0.521 and 0.700 MeV	196
Figure 7.17	Comparison of electron and contamination depth dose curves from Monte Carlo calculations on radiographic film using the different AE for a 6 MV beam with a field size of 20 x 20 cm ² : a) AE = 0.521 MeV, b) AE = 0.700 MeV, c) AE = 0.521 and 0.700 MeV	197
Figure 7.18	Comparison of electron depth dose curves from Monte Carlo calculations on radiographic film using the different AE: a) AE = 0.521 MeV for F.S. 10 x 10 and 20 x 20 cm ² , b) AE = 0.700 MeV for F.S.10 x 10 and 20 x 20 cm ² , c) AE = 0.521 and 0.700 MeV for F.S.10 x 10 and 20 x 20 cm ²	198
Figure 7.19	Comparison of contamination dose distribution curves from Monte Carlo calculations on radiographic film using the different AE: a) AE = 0.521 MeV for F.S. 10 x 10 and 20 x 20 cm ² , b) AE = 0.700 MeV for F.S.10 x 10 and 20 x 20 cm ² , c) AE = 0.521 and 0.700 MeV for F.S.10 x 10 and 20 x 20 cm ²	199
Figure 8.1	Extrapolated surface dose profile at central axis for 6 MV beam, measured cross-plane and in-plane: a) without (open field) magnetic field from the deflector for field sizes of 5 x 5 cm ² , 10 x	205

10 cm², 20 x 20 cm², and 30 x 25 cm², b) with magnetic field from the deflector for field sizes of 5 x 5 cm², 10 x 10 cm², 20 x 20 cm², and 30 x 25 cm²

- | | | |
|------------|---|-----|
| Figure 8.2 | Schematic diagram of the Monte Carlo model used to simulate the Varian Clinac 2100 C for 6 MV x-ray beams | 207 |
| Figure 8.3 | The geometry of the Clinac 2100 C accelerator head for 6 MV photon beam as shown by EGS_Windows 4.0 using 150-200 histories. Photons are represented by yellow lines, and electrons are represented by blue lines | 208 |

LIST OF TABLES

Table 2.1	Comparison of surface dose as a function of field size for several linear accelerator models	7
Table 2.2	Percentage surface dose for linear accelerators measured at SSD 100 cm for 10 x 10 cm ² field size using an extrapolation chamber	8
Table 2.3	Percentage skin dose of 8 and 18 MV x-ray beams for different field sizes and wedge angles	22
Table 2.4	The sources of electron contamination in the 25 MV Clinac-35 photon beam for different SSD distances	23
Table 4.1	The electron deflection in magnetic field for electron energies ranging from 6 MeV up to 20 MeV	82
Table 4.2	Surface dose measurements by the extrapolation technique from radiographic film compared to the Attix chamber results for 6 MV x-rays with and without (open field) magnetic field from the deflector	100
Table 5.1	Surface doses for field sizes of 15 x 15 cm ² and 20 x 20 cm ² for 6 MV x-rays using radiographic film combined with a wedge and magnetic field	124
Table 5.2	Surface dose for field size of 20 x 20 cm ² with a Perspex tray and with different wedges used with and without magnetic field	125
Table 5.3	Surface dose measurements by an Attix chamber and extrapolated from radiographic film for field sizes of 10 x 10 cm ² , 15 x 15 cm ² , and 20 x 20 cm ²	126
Table 6.1	The description of the accelerator geometry is provided by the manufacturer	136
Table 6.2	Fluence-averaged quantities for first-time crossing of the scoring plane normalised per incident particles	155
Table 6.3	Number and energy fluence distributions of 6 MeV electron beams from Varian Clinac 2100 C linear accelerator	156
Table 6.4	Angular distributions of photons and particles	156

Table 6.5	The depth dose distribution on the central axis of 6 MV Clinac 2100 C for field size of 10 x 10 cm ² using AE = 0.521 and 0.700 MeV at the same depth in a water phantom	167
Table 6.6	The dose profile distribution of 6 MV Clinac 2100 C for field size of 10 x 10 cm ² using AE = 0.521 and 0.700 MeV at the same depth in a water phantom along the X and Y-axes	169
Table 7.1	DOSXYZnrc simulation parameters	177
Table 7.2	(a) Percentage of the dose in the build-up region between experimental data and Monte Carlo calculations for 6 MV beam in a water phantom and radiographic film for AE = 0.700 MeV of field size 10 x 10 cm ² and 20 x 20 cm ²	180
	(b) Percentage of the dose in the build-up region between experimental data and Extrapolated surface dose of Monte Carlo calculations for 6 MV beam in a water phantom for AE = 0.700 MeV of field size 10 x 10 cm ² and 20 x 20 cm ² .	180
Table 7.3	Percentage of the surface dose from Monte Carlo calculations compared to the measurements on radiographic film	194
Table 8.1	Percentage of dose from the contamination and the percentage reduction for field sizes of 10 x 10 cm ² , 15 x 15 cm ² , and 20 x 20 cm ² with the magnetic deflector device in place for a 6 MV x-ray beam in the build-up region	203
Table 8.2	Percentage of dose absorbed at the surface for field sizes of 10 x 10 cm ² , 15 x 15 cm ² , and 20 x 20 cm ² with the use of beam modifying devices and the magnetic deflector device in place for 6 MV x-ray beam from radiographic film	204

ACKNOWLEDGEMENTS

My sincere thanks go to everyone who has assisted and supported me throughout the three and a half years of this PhD project.

To The Royal Thai Government for providing me scholarships.

To my supervisors, Professor Anatoly Rosenfeld and A/Prof. Martin Butson, for your encouragement and guidance throughout the difficult situations. I am very grateful and appreciative for your tremendous academic and personal support, without you this work would not be possible. Also, I would like to thank Professor Peter Metcalfe and Dr George Takacs, for your support and advice.

Thanks to Puangpen Tangboonduangjit, Brad Oborn and friends in the Centre for Medical Radiation Physics and also friends in School of Engineering for the support and friendship.

Finally, to my dad and mum and my sister with highly respect who have greatly cared, constantly supported, and been next to me no matter what circumstances. This thesis is dedicated to them.